Front. Mater. Sci. 2020, 14(2): 120–132
https://doi.org/10.1007/s11706-020-0499-3

RESEARCH ARTICLE

Facile solvothermal synthesis of $NiFe_2O_4$ nanoparticles for high-performance supercapacitor applications

Meenaketan SETHI[1], U. Sandhya SHENOY[2], Selvakumar MUTHU[3], and D. Krishna BHAT (✉)[1]

1 Department of Chemistry, National Institute of Technology Karnataka, Surathkal, Mangalore-575025, India
2 Department of Chemistry, College of Engineering and Technology, Srinivas University, Mukka-574146, Karnataka, India
3 Department of Chemistry, Manipal Institute of Technology, Manipal-576104, Karnataka, India

ABSTRACT: We report a green and facile approach for the synthesis of $NiFe_2O_4$ (NF) nanoparticles with good crystallinity. The prepared materials are studied by various techniques in order to know their phase structure, crystallinity, morphology and elemental state. The BET analysis revealed a high surface area of 80.0 $m^2 \cdot g^{-1}$ for NF possessing a high pore volume of 0.54 $cm^3 \cdot g^{-1}$, also contributing to the amelioration of the electrochemical performance. The NF sample is studied for its application in supercapacitors in an aqueous 2 $mol \cdot L^{-1}$ KOH electrolyte. Electrochemical properties are studied both in the three-electrode method and in a symmetrical supercapacitor cell. Results show a high specific capacitance of 478.0 $F \cdot g^{-1}$ from the CV curve at an applied scan rate of 5 $mV \cdot s^{-1}$ and 368.0 $F \cdot g^{-1}$ from the GCD analysis at a current density of 1 $A \cdot g^{-1}$ for the NF electrode. Further, the material exhibited an 88% retention of its specific capacitance after continuous 10000 cycles at a higher applied current density of 8 $A \cdot g^{-1}$. These encouraging properties of NF nanoparticles suggest the practical applicability in high-performance supercapacitors.

KEYWORDS: $NiFe_2O_4$; nanoparticle; solvothermal method; BET surface area; specific capacitance; supercapacitor

Contents

Received December 12, 2019; accepted February 6, 2020

E-mail: denthajekb@gmail.com

1 Introduction

The modern world is in need of vast energy storage systems to cater to the demands of the domestic, public and

industrial establishments at a large scale. In view of this, energy storage devices are paid a great attention as they have high storing capacity, fast charging and discharging ability, high rechargeability and hence, they can be used for various applications [1]. Although batteries are used for the storage of large amount of charge, they lack fast charging and high cyclability. Tethering batteries with supercapacitors can ameliorate the charge storage capacity and can be used for future energy storage devices. The charge storage mechanism decides the category of the supercapacitor i.e., electrochemical double-layer capacitor (EDLC) or pseudocapacitor. In EDLCs, generally carbonaceous materials of high surface area is used as electrode material, as EDLC phenomena is dependent on the electrode/electrolyte interface where ion transport takes place and leads to the creation of an electrochemically active double layer [2–3]. In pseudocapacitors, the charge is developed by the faradaic redox reactions at the electrode surface; this property is generally shown by oxides and sulphides of metals/polymers [4]. Among oxides of metals, RuO_2 is considered as the best electrode material for supercapacitor application, but the cost and toxicity issues limit its applicability. Recently mixed metal oxides/spinels are considered as superior electrode materials for supercapacitors as compared to the single oxides owing to the mixture of two metal domains, various oxidation states, easy synthesis and high electrochemical response. Among the spinels, $NiCo_2O_4$ has exhibited good electrochemical activity due to its high electrical conductivity [5–6]. But the other spinels such as $ZnCo_2O_4$, $MnCo_2O_4$, $CoFe_2O_4$ and $NiFe_2O_4$ (NF) are less studied owing to their inadequate electrical conductivity [7–8]. There are many studies on the synthesis of NF nanostructures by mainly hydrothermal and wet chemical methods and a few by sol-gel method [8–15]. But the electrochemical study of thus synthesized NF reported very less specific capacitance value ranging from 95 to 350 $F \cdot g^{-1}$ [13–14]. Wherever high values were reported ranging from 435 to 677 $F \cdot g^{-1}$, it was due to the usage of Ni foam or high concentration of KOH (6 mol $\cdot L^{-1}$), which are not desirable for a low cost and facile experimentation [11]. In some cases, where the capacitance values were of the order of 342–562 $F \cdot g^{-1}$, the capacitance retention ability was very low even for 1000 cycles making it unsuitable for commercialization [12–13]. Hence, there is a requisite to synthesize NF by a facile method such that it exhibits high value of supercapacitance without using Ni foam or high concentration of KOH and systematically study its electrochemical activities.

Hence, in the present study, we report the synthesis of NF nanoparticles using 1:1 water and ethylene glycol. The synthesis employing mixed solvent mediated route is a simple low-temperature solvothermal approach and yields material with high capacitance value and high life cycle. We studied the as-prepared NF nanoparticles for their electrochemical response for utilization as supercapacitor electrode material. When the electrode material is tested in aqueous 2 $mol \cdot L^{-1}$ KOH electrolyte, we obtained a high capacitance value of 478 $F \cdot g^{-1}$ at a scan rate of 5 $mV \cdot s^{-1}$. The electrode material also exhibited good capacitance retention value of 88% after continuous 10000 cycles at a high current density of 8 $A \cdot g^{-1}$. The better electrochemical performance displayed by the electrode is primarily attributed to the nano dimension and good surface area along with mesoporous structure and large pore volume of NF. The facile synthetic route, high capacitance value in low concentration of KOH and absence of expensive current collectors like Ni foam makes the material potent to be used as electrode material in supercapacitors.

2 Methods

2.1 Synthesis of NF nanoparticles

All chemicals used are of analytical grade and are used without further purification. Deionized water is used wherever required for the synthesis of materials and for washing of the materials. NF is synthesised by solvothermal method using mixed solvents. First, $Ni(NO_3)_2 \cdot 6H_2O$ and $Fe(NO_3)_3 \cdot 9H_2O$ (1:2 mmol) are dissolved in 50 mL (1:1 mixture, deionised water + ethylene glycol) and it is sonicated in a bath sonicator for 30 min to ensure complete dissolution. Urea (9 mmol) is added to the mixture while stirring and the solution is kept stirred continuously for one hour to obtain homogeneity, which is then added to a Teflon lined stainless steel autoclave and heated for 18 h at a temperature of 160 °C. Then, the autoclave is brought to room temperature gradually. The obtained brown color product is washed several times with deionized water followed by ethanol till we get neutral pH, after which it is dried at 70 °C. Later it is calcined at 400 °C for 2 h in air to get pure NF nanoparticles.

2.2 Materials characterization

The X-ray diffraction (XRD) data in the range of 20°–80°, used to determine the crystal and phase structure of the synthesized sample, are obtained at a scan rate of 2(°)/min

using monochromatic Cu Kα radiation (0.154 nm wavelength) on Rigaku (Japan) instrument. The Raman analysis is carried out using Lab Ram HR instrument (Airix Corp.) with the use of 532 nm laser source. The morphology and elemental constitutents are examined by field-emission scanning electron microscopy (FESEM), energy dispersive X-ray analysis (EDX) and transmission electron microscopy (TEM) using ZEISS Ultra Plus 55 field-emission scanning electron microscope, Oxford instruments and Fei Tecnai G2 instrument, respectively. The surface area of the material is tested using BEL SORP II Japan instrument. Prior to the analysis, the samples are degassed at 200 °C in vacuum for 2 h.

2.3 Electrode preparation for supercapacitor application

The supercapacitor electrodes are prepared by mixing NF nanoparticles, poly(vinylidene fluoride) binder and acetylene black in 8:1:1 weight ratio in a mortar and pestle to make a slurry like ink [16]. Then, by following Doctor's blade technique, the ink paste is coated on one side of the polished Ni sheet of 1 cm^2 area and further heated at 80 °C for 12 h in order to evaporate the solvent. The weight deposited is found to be ~1 mg after measuring the electrodes carefully in an analytical balance of readability 0.0001 g. The electrochemical characterization is performed by using a three-electrode cell system with the NF-coated Ni sheet as working electrode, saturated calomel electrode (SCE) as reference, platinum wire as counter electrode, and 2 $mol \cdot L^{-1}$ KOH as electrolyte. The electrochemical characterizations such as cyclic voltammetry (CV), galvanostatic charge–discharge measurement (GCD) and electrochemical impedance spectroscopy (EIS) are carried out by using electrochemical workstation (IVIUM Technologies BV Co., the Netherlands, Model: Vertex).

2.4 Supercapacitor device fabrication

The supercapacitor device is fabricated following previous literature [5,16]. The slurry like paste is prepared by following the procedure reported in previous section [16]. Then, the paste is coated on one side of Toray carbon paper of area 2 cm × 2 cm by using brush coating method and dried at 80 °C overnight in order to remove the solvent. The deposited mass is calculated after drying of the cabon paper and is found to be ~3 mg per carbon paper as measured in an analytical balance of readability 0.0001 g. The supercapacitor cell consists of NF coated carbon paper as electrodes, Whatman filter paper wetted in 2 $mol \cdot L^{-1}$ KOH as a separator, and 306 grade stainless steel sheets as current collectors. The filter paper is sandwiched between the two electrodes, and again it is sandwiched between the current collectors. The EIS study for both single electrode and supercapacitor device is done in the applied frequency range from 10^5 Hz to 0.01 Hz using an alternative current (AC) perturbation of 10 mV.

The specific capacitance (C_s, unit: $F \cdot g^{-1}$) values from CV graphs are calculated using Eq. (1):

$$C_s = \frac{nA}{\Delta V \times m \times \nu} \tag{1}$$

where A is the integrated area of the CV curve, v (unit: $V \cdot s^{-1}$) is the applied scan rate, m (unit: g) is the deposited mass on one single electrode, and ΔV (unit: V) is the operated potential window. A factor of $n = 2$ is multiplied owing to the formation of series capacitance in a symmetrical supercapacitor device and for the three-electrode system we consider, $n = 1$.

The specific capacitance (C_s, unit: $F \cdot g^{-1}$) values from GCD graphs are calculated using Eq. (2):

$$C_s = n \times \frac{I \times \Delta t}{m \times \Delta V} \tag{2}$$

where I/m (unit: $A \cdot g^{-1}$) is the applied current density, Δt (unit: s) is the discharging time, ΔV (unit: V) is the maximum potential window to discharge the cell, and $n = 2$ for symmetrical supercapacitor device and $n = 1$ for the three-electrode system.

The energy density (E, unit: $W \cdot h \cdot kg^{-1}$) and power density (P, unit: $W \cdot kg^{-1}$) for the prepared electrode are calculated according to Eqs. (3) and (4), respectively [17]:

$$E = \frac{1}{2} \times C_s \times \Delta V^2 \times \frac{1000}{3600} \tag{3}$$

$$P = \frac{E_{app}}{t_d} \times 3600 \tag{4}$$

where, C_s (unit: $F \cdot g^{-1}$) is the specific capacitance, ΔV (unit: V) is the maximum potential window, E_{app} (unit: $W \cdot h \cdot kg^{-1}$) is the applied energy density, and t_d (unit: s) is the discharging time. For the fabricated symmetrical supercapacitor, the term 1/2 in Eq. (3) is replaced with 1/8 for the calculation of energy density [17].

2.5 Computational section

The electronic structure of NF was determined within first-principles density functional theory (DFT) based calcula-

tions using Quantum ESPRESSO package with scalar relativistic ultrasoft pseudopotentials and exchange-correlation energy functional of Perdew–Burke–Ernzerhof (PBE) [18–19]. $3d^84s^2$, $3d^64s^2$ and $2s^22p^4$ configurations were considered as valence electrons for Ni, Fe and O respectively within a generalized gradient approximation. Inverse spinel structure of NF was simulated using fully relaxed structure. The crystal structure was relaxed to minimize the energy until the magnitude of Hellman–Feynman force on each atom was less than 0.01 $eV \cdot Å^{-1}$, and the magnitude of stresses within 1 kbar. Plane wave basis sets representing wavefunctions and charge density were truncated at energy cut-offs of 50 and 400 Ry, respectively. A $8\times8\times8$ mesh of k points for scf and $16\times16\times16$ mesh for nscf calculations were used to sample integrations over the Brillouin zone. Electronic structure was determined along Γ-X-M-Γ-R-X path in the Brillouin zone [20].

3 Results and discussion

3.1 XRD and Raman analysis

The phase and crystallinity of the as-synthesized NF are analyzed by XRD. Figure 1(a) shows the XRD pattern of NF with standard data (JCPDS card No. # 074-2081). The XRD peaks show the crystalline nature of the material with broadened base suggesting the nano dimension of the synthesized NF. The absence of any other kind of peaks in the XRD pattern suggests the formation and high purity of the sample. The average crystal size is determined from the highest intensity peak from the (3 1 1) crystal plane by using Debye-Scherrer's equation and the crystallite size is found to be around 17 nm.

Raman spectra of NF nanoparticles (Fig. 1(b)) showed five Raman actives modes i.e., $A_{1g} + E_g + 3T_{2g}$ modes according to the group theory calculations [9,21–23]. The T_{2g} mode possesses three Raman bands including 206, 483 and 562 cm^{-1}. The bands at 321 and 692 cm^{-1} are assigned to E_g and A_{1g} modes, respectively. Raman signal of cubic NF at 692 cm^{-1} is attributed to the A_{1g} symmetry of oxygen in tetrahedral group, while the other modes describe the octahedral sites. Raman spectrum shows three different kinds of vibrational modes in the lattice. The A_{1g} mode arises due to the symmetric stretching of O atoms with Ni–O and Fe–O bonds in a tetrahedral structure. The three T_{2g} modes are generated due to the asymmetric stretching of Ni/Fe/O and asymmetric bending of O relative to the metal ion. The E_g mode is symmetric bending of O atom relative to the metal ion.

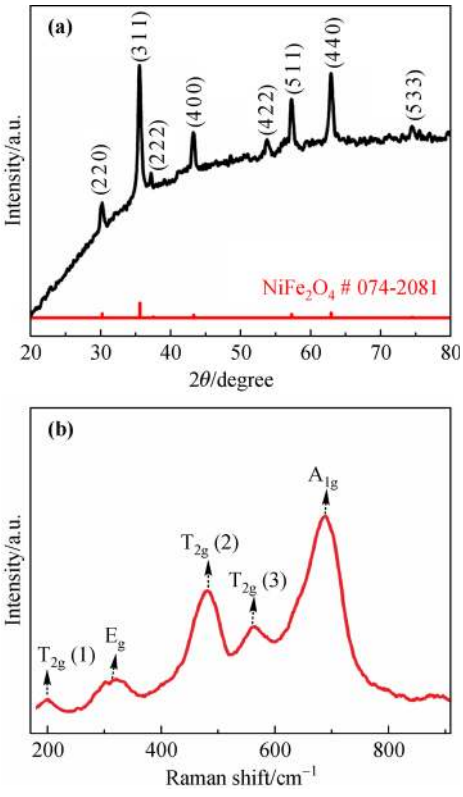

Fig. 1 **(a)** XRD pattern of NF with the standard data. **(b)** Raman spectrum of NF nanoparticles.

3.2 Morphological and surface area analysis

The mixed solvent solvothermal approach led to the formation of uniformly distributed spherical nanoparticles as revealed by FESEM image of the size from 13 to 17 nm (Fig. 2(a)). The EDX shows the presence of Ni, Fe and O as elemental constituents (Fig. 2(b)). The presence of C peak is due to the carbon tape used during analysis. The observed atomic ratio of elements Ni, Fe and O in the sample is found to be approximately 1:2:4, supporting the formation of NF. The pores within NF nanoparticles are seen in the TEM images (Figs. 2(c) and 2(d)). The measured interplanar distance in the high-resolution transmission electron microscopy (HRTEM) image (Fig. 2(e)) matches with (3 1 1) and (4 2 2) crystal planes of NF. The selected area electron diffraction (SAED) patterns show well formed concentric rings, depicting the polycrystalline nature of NF (Fig. 2(f)). The concentric rings correlate well with the XRD pattern of NF nanoparticles, which further supports the formation of NF.

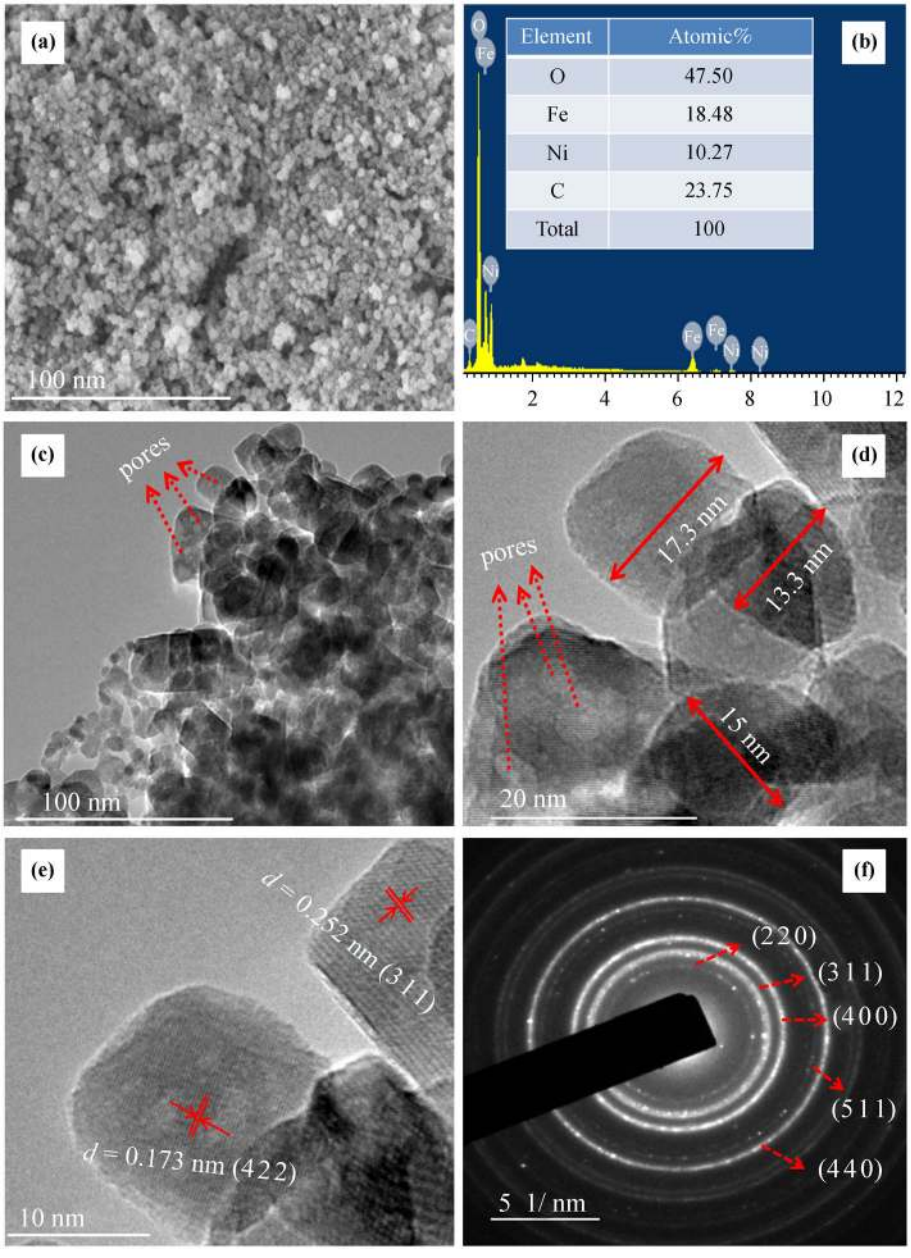

Fig. 2 **(a)** FESEM image, **(b)** EDX data (inset shows the elemental composition), **(c)** low magnification TEM image, **(d)** high magnification TEM image, **(e)** HRTEM image with the measured interplanar distance matching with (4 2 2) and (3 1 1) crystal planes and **(f)** SAED pattern of NF nanoparticles.

The Brunauer–Emmett–Teller (BET) surface area analysis is a prominent measurement tool to obtain information about the specific surface area value along with the pore volume and pore diameter [23]. The BET plot determined is shown in Fig. 3, and it belongs to type-IV class of isotherms. This kind of isotherm with H3 hysteresis loop is in general suggestive of porous nature of the material. The measured BET surface area of NF nanoparticles is 80 $m^2 \cdot g^{-1}$, seeming to be higher than previously reported values of NF nanoparticles (76.9 $m^2 \cdot g^{-1}$), nano sheets (47 $m^2 \cdot g^{-1}$), nano flower (25 $m^2 \cdot g^{-1}$), nano feather (11 $m^2 \cdot g^{-1}$), NF nanomaterials (0.968 $m^2 \cdot g^{-1}$), NF/RGO composite (57.3 $m^2 \cdot g^{-1}$), NF nanoarchitectures (73.1 $m^2 \cdot g^{-1}$), nanocrystals (39.1 $m^2 \cdot g^{-1}$), and NF nanoparticles (76.2 $m^2 \cdot g^{-1}$) [10–11,14,24–26]. Also, the Barrett–Joyner–Halenda (BJH) plot analysis revealed a large pore volume of 0.54 $cc \cdot g^{-1}$ and mesoporous nature of the material. The total supercapacitance of a material is the sum of double layer capacitance and quantum capacitance [16]. The

double layer capacitance is dependent on the surface area and morphology of the electrode material. Hence, nano structures with high surface area is believed to contribute towards enhancement of electrochemical properties and therefore is highly suitable for charge storage applications [27–28].

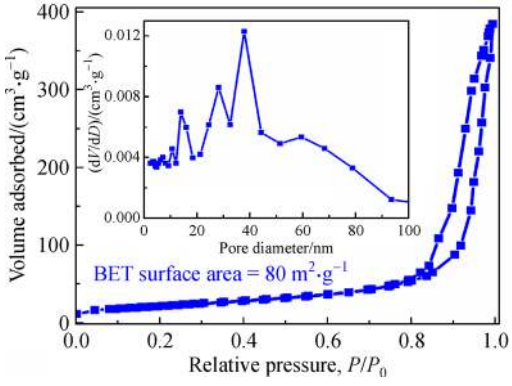

Fig. 3 The BET surface area plot of NF (inset showing the BJH plot).

3.3 DFT analysis

NF belongs to a class of materials which are called spinels with the general formula AB_2O_4. In this class of materials metal ions occupy the tetrahedral and octahedral sites created by the oxygen face centred cubic (FCC) lattice. The degree of inversion is decided by the factor x which can have the value of 0 or 1, in the composition indicated by $(A_{1-x}B_x)^{2+}(A_xB_{2-x})^{3+}O_4$. In normal spinels with $x = 0$, the divalent cations occupy the tetrahedral site while the octahedral sites are occupied by the trivalent cations. In inverse spinels with $x = 1$, the divalent cations occupy the octahedral site while the trivalent ions are equally distributed between the tetrahedral and octahedral sites. Bulk NF has inverse spinel structure and hence is simulated by arranging Ni^{2+} ions in octahedral sites along with half of Fe^{3+} ions, while the rest half of the Fe^{3+} ions occupy the tetrahedral sites (Fig. 4).

The electronic structure of the material largely decides its quantum capacitance. The increase in the electronic density of states near the Fermi level improves the quantum capacitance and in turn the total capacitance. The electronic structure of NF in Fig. 5(a) reveals a deep valence band (VB), a dense upper VB, a dense lower conduction band (CB) and a diffuse upper CB. The curvature of the bands decide the effective mass of the charge carriers and in turn the electrical conductivity. Flat bands have low conductivity while bands with high curvature favor high electrical

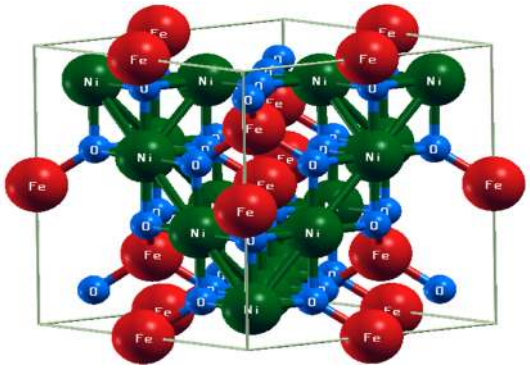

Fig. 4 The crystal structure of NF (Ni, Fe and O are represented by green, red and blue spheres, respectively).

conductivity [29]. Also, for a material to act as a supercapacitor the necessary condition is that the electronic structure should have occupied states near the Fermi level [16]. Herein, we see that the Fermi level occurs at the edge of the VB with high occupancy and thus we can predict a better supercapacitance behaviour. When we project the atomic orbitals onto the density of states (DOS) to study the orbital contribution to the electronic structure we observe that the deep VB is constituted majorly by the O 'p' orbitals and the upper CB is formed by Ni 's' orbitals indicating the ionic nature of Ni. The partial density of states (pDOS) on either side of Fermi level reveal that upper VB predominantly consists of 'd' states of Ni and Fe while the CB is primarily constituted by O 'p' orbitals hybridized with 'd' orbitals of Ni and Fe (Fig. 5(b)). The severe under estimation of band gap of NF is well known due to the strong coupling between 'd' and 'p' states of the orbitals forming VB and CB.

The variation of DOS and electrical conductivity of NF as a function of temperature in the range from 300 to 800 K was determined using Boltztrap code employing semi-classical Boltzmann theory under a constant scattering time approximation (Figs. 5(c) and 5(d)). The chemical potentials ranging from negative to positive values indicate hole and electron doping representing the p- and the n-type, respectively [30–31]. Since relaxation time is an undetermined quantity, the electrical conductivity is reported as σ/τ. It is observed that around the Fermi level the electrical conductivity is independent of temperature as the DOS is nearly independent of temperature from 0 to -0.5 eV [29]. Further, as we increase or decrease the potential the conductivity decreases with increase in temperature. On either side of Fermi level around $+0.7$ and -0.4 eV there is sharp peak in the conductivity values indicating the potential which can be best exploited for increasing the

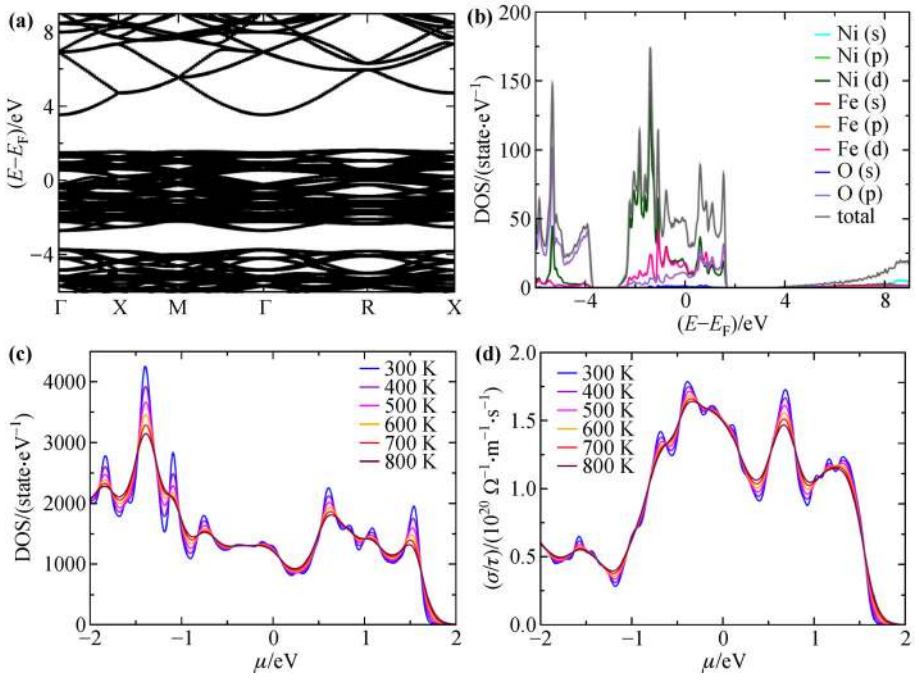

Fig. 5 **(a)** Electronic structure and **(b)** pDOS of NF. **(c)** DOS and **(d)** electrical conductivity (σ/τ) as a function of chemical potential (μ) and temperature.

conductivity and in turn improve the supercapacitance of the material [16].

3.4 The three-electrode method of electrochemical analysis

The electrochemical analyses of the NF electrodes are carried out using a three-electrode method with 2 mol·L^{-1} KOH as electrolyte. The CV, GCD and EIS measurements are made for the evaluation of electrochemical properties of NF nanoparticles (Fig. 6). Figure 6(a) shows CV curves of NF at varying scan rates ranging from 5 to 100 mV·s^{-1}, which are typically of pseudocapacitive nature, showing a redox peak pair in the anodic and cathodic sweeps. The anodic part of the CV curve is asymmetric in nature. It is well known that the peaks are representative of reversible charge transfer reactions taking place on the material surface and obviously, in NF sample, faradic charge storage mechanism dominates over electrostatic charge storage mechanism. Thus, the major contribution to the capacitance of the sample is from pseudocapacitance due to reversible electrochemical reactions associated with [Ni/Fe]–O/[Ni/Fe]–O–OH [32]. The observed asymmetric trait in the anodic peak of the CV curve is attributed to these processes. The calculated specific capacitance values are 478, 409, 289, 263, 203, 188 and 176 F·g^{-1} for the scan rates of 5, 10, 20, 30, 50, 75 and 100 mV·s^{-1}, respectively. The GCD curves of NF at different current densities in the range from 1 to 16 A·g^{-1} are displayed in Fig. 6(b). The pseudocapacitive GCD curves with symmetrical loops are of high significance in the supercapacitor application. The high discharging time of the electrode material resulted in high specific capacitance values [33]. The capacitance value decreases from 368 F·g^{-1} at a current density of 1 A·g^{-1} to 266 F·g^{-1} at a current density of 16 A·g^{-1}. A high power density of 3375.0 W·kg^{-1} is obtained for the material while maintaing an energy density of 7.5 W·h·kg^{-1} at a current density of 16 A·g^{-1}.

The reported specific capacitance values in 2 mol·L^{-1} KOH electrolyte, from the CV and GCD curves, are high as compared to previous reported literature, and are summarized in Table 1 [8,10–12,14,34].

Figure 6(c) shows the electrochemical impedance spectra in the form of Nyquist plot of NF in 2 mol·L^{-1} KOH electrolyte in the frequency range from 10^5 Hz to 0.01 Hz. From this figure, it is evident that the material has good electrochemical characteristics such as high capacitance and conductivity. As can be seen from the inset of Fig. 6(c), there is no semicircle in the high frequency region indicating low R_s and R_{ct} values. An almost flat tail nearly parallel to the Z''-axis (imaginary axis) in the low-frequency region suggests the faster kinetics and ideal capacitive nature of the material. These features may be

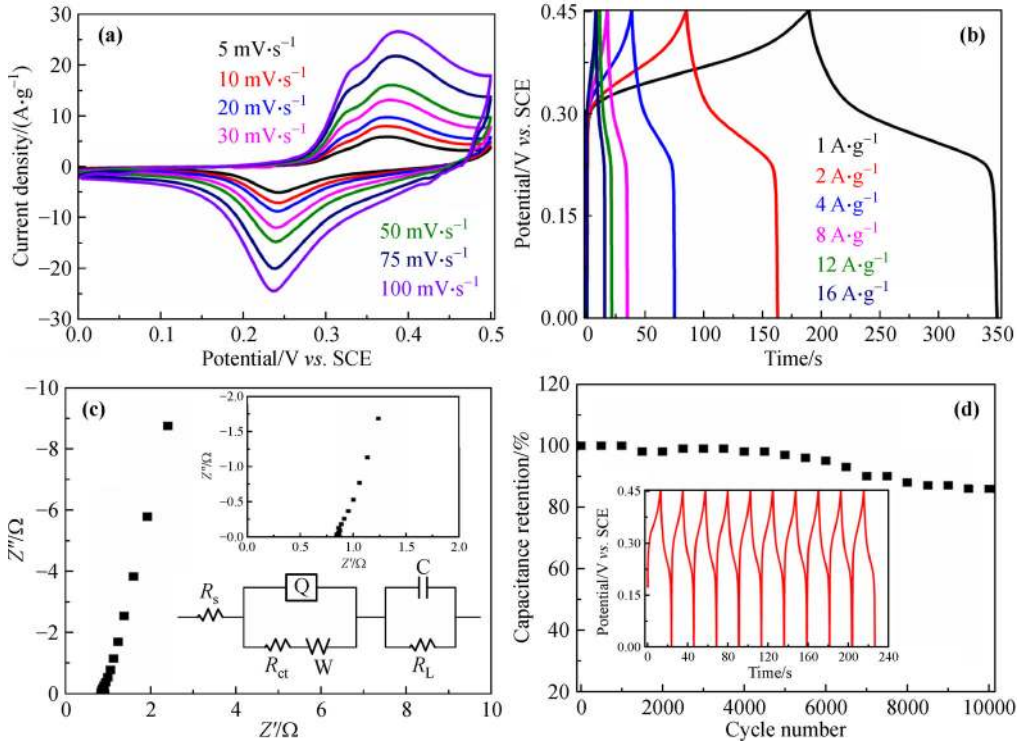

Fig. 6 Electrochemical analysis of NF in a three-electrode system: **(a)** CV curves; **(b)** GCD curves; **(c)** Nyquist plot (inset showing high-frequency region and fitted equivalent circuit) and **(d)** cyclic stability data of NF for 10000 discharge cycles at a constant current density of 8 A·g^{-1} in 2 mol·L^{-1} KOH electrolyte (inset showing the first 10 cycles).

attributed to the nanoparticle structure with high surface area and large pore volume. In the equivalent circuit (inset of Fig. 6(c)), the constant phase element (Q) along with the charge-transfer resistance (R_{ct}) is in series connection with the solution resistance (R_s). The Warburg element (W) is connected in series with R_{ct}. The vertical line in the low frequency region, which is nearly parallel to the imaginary axis (Z'' axis) is slightly deviated from its ideal capacitive nature due to the parallel connection of leakage current (R_L) with the capacitive element (C). The obtained value of R_s is 0.76 Ω.

The superior electrochemical performance is again tested for cyclic stability for continuous 10000 cycles at a high current density of 8 A·g^{-1}. The structure of NF is such that it is able to sustain a rapid electron insertion/de-insertion process and in addition to that the high pore volume allowed the electrolyte ions to move freely across the bulk into the interior of the particles. The cyclic stability test (Fig. 6(d)), clearly indicates that the electrode maintains its initial value up to 1500 cycles, thereafter the values slightly decrease. After large number of cycles, the particle aggregation may create hindrance to the transport of the ions inside the pores, which ultimately decreases the capacitance retention ability. The TEM image of NF particles after 10000 cycles is shown in Fig. 7. At an applied current density of 8 A·g^{-1}, 88% initial capacitance value is retained even after 10000 cycles for the NF electrode material, which is higher than the reported NF and graphene/NF electrode material [8,10–14,34]. The capacitance retention values are compared and tabulated in Table 1.

3.5 Electrochemical analysis of the fabricated symmetrical supercapacitor

The electrochemical performance of the fabricated supercapacitor is displayed in Fig. 8. The CV curves at the scan rates ranging from 2 to 100 mV·s^{-1} are rectangular in shape indicating a signature of good electrochemical performance of the material and are suitable for supercapacitor application (Fig. 8(a)) [16]. The calculated specific capacitance values are 89, 77, 71, 64, 58 and 45 F·g^{-1} for the scan rates ranging from 2 to 100 mV·s^{-1}. The GCD studies for the current densities ranging from 0.5 to 8 A·g^{-1} are displayed in Fig. 8(b) and the symmetrical nature is an indication of good capacitive property.

The Nyquist plot of the fabricated supercapacitor is displayed in Fig. 8(c), which shows a semicircle in the

Table 1 Comparison of electrochemical properties of NF nanoparticles from this work with other reported NF nanostructures and graphene/$NiFe_2O_4$ composites in the three-electrode set-up [8,10–12,14,34]

Electrode material	Specific capacitance @scan rate	Specific capacitance @current density	Electrolyte	Cyclic stability	Refs.
NF nanoparticles	478 $F \cdot g^{-1}$@5 $mV \cdot s^{-1}$	368 $F \cdot g^{-1}$@1 $A \cdot g^{-1}$	2 $mol \cdot L^{-1}$ KOH	88% after 10000 cycles @8 $A \cdot g^{-1}$	this work
NF nanoassemblies	109.2 $F \cdot g^{-1}$@2 $mV \cdot s^{-1}$	–	3 $mol \cdot L^{-1}$ KOH	>90% after 1000 cycles@10 $mV \cdot s^{-1}$	[8]
NF nanoparticles	–	174 $F \cdot g^{-1}$@1 $A \cdot g^{-1}$	1 $mol \cdot L^{-1}$ KOH	130% after 2000 cycles @1 $A \cdot g^{-1}$	[10]
NF nanoflowers	–	435 $F \cdot g^{-1}$@5 $mA \cdot cm^{-2}$	6 $mol \cdot L^{-1}$ KOH	80% after 7000 cycles	[11]
NF nanocrystals	–	562 $F \cdot g^{-1}$	2 $mol \cdot L^{-1}$ KOH	84% after 1000 cycles @4 $A \cdot g^{-1}$	[12]
NF nanoparticles	97.5 $F \cdot g^{-1}$@2 $mV \cdot s^{-1}$	–	0.1 $mol \cdot L^{-1}$ NaCl	100% after 100 cycles @5 $mV \cdot s^{-1}$	[14]
NF nanocubes	–	325 $F \cdot g^{-1}$@3 $A \cdot g^{-1}$	1 $mol \cdot L^{-1}$ KNO_3	78.9% after 10000 cycles@3 $A \cdot g^{-1}$	[34]

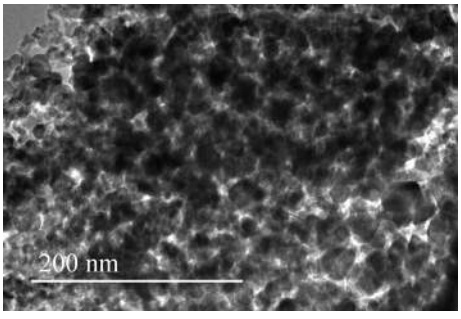

Fig. 7 TEM image of NF nanoparticles after 10000 cycles.

high-frequency region, and the large arc displayed in the figure is related to the resistance offered by the symmetrical cell. The best fitted equivalent circuit is shown in the inset of Fig. 8(c), where the intercept on the real (Z') axis corresponds to the solution resistance (R_s), consisting of the resistance offered by the electroactive material, electrolyte solution and contact between the electroactive material/current collector interface. The obtained R_s is 1.25 Ω. The charge transfer resistance (R_{ct}) and double-layer capacitance (C_{dl}) of the supercapacitor are indicated by the arc exhibited by the device in the high-frequency region and the obtained R_{ct} value is 35.6 Ω. The line making an angle 45° in the low-frequency region is known as the Warburg impedance (W), generated owing to the diffusion/transport of OH^- ions into the electroactive material [17].

The cyclic stability study for the symmetrical supercapacitor is performed for 10000 cycles at a higher applied current density of 8 $A \cdot g^{-1}$ (Fig. 8(d)). After the 10000th cycle the cell was able to retain 81% of its initial capacitance. The decrease in the retention value may be due to the particle agglomeration, drying of electrolyte owing to which the electrolyte ions cannot pass through the inner pores and interact only at the surface. The calculated energy density and power density values from GCD curves of the three-electrode system and symmetrical supercapacitor are graphically given in Fig. 9. Also, the obtained capacitance value for the supercapacitor cell is compared with recently reported literature, and all of them are presented in Table 2 [11,34–37].

The admittance plot for the single electrode and supercapacitor device are displayed in Fig. 10. By estimating the knee frequency value (f_o), the time constant (τ_0) value can be calculated using Eq. (5):

$$\tau_0 = \frac{1}{\log f_o} \tag{5}$$

The calculated time constant value for the single electrode is 0.4 ms and that for supercapacitor device is 10 ms. The obtained high capacitance values are supported by low time constant values.

The participation of surface reactive sites (Z) in the course of the redox process of NF can be computed by using Eq. (6):

$$Z = \frac{MC_s\Delta V}{F} \tag{6}$$

where, M is the molecular mass of $NiFe_2O_4$ (236.395 g $\cdot mol^{-1}$), ΔV (unit: V) is the potential window, C_s (unit: F $\cdot g^{-1}$) is the specific capacitance (obtained from CV curve) and F is the faraday constant (96485 $C \cdot mol^{-1}$). The obtained value of Z for the single electrode is 0.50 and that for supercapacitor device is 0.22. The Z value decides the number of electroactive sites participating in the electrochemical redox reaction and it will be equal to 1 if all the

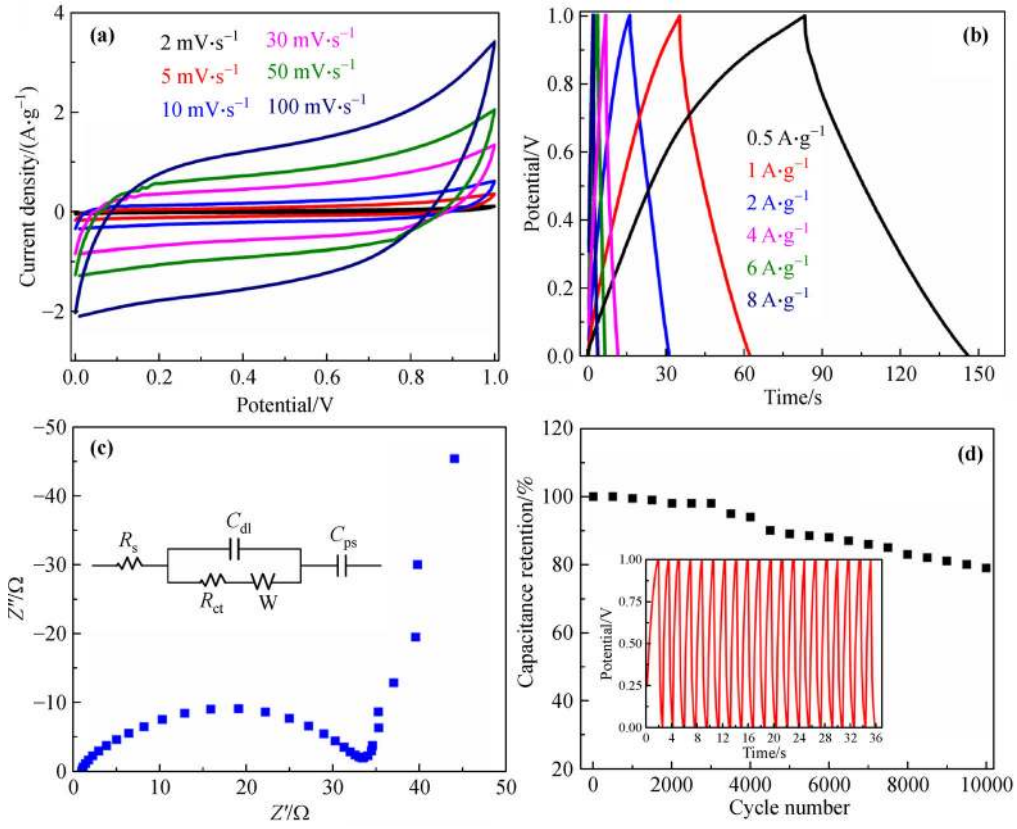

Fig. 8 Electrochemical analysis of the fabricated supercapacitor device: **(a)** CV curves; **(b)** GCD curves; **(c)** Nyquist plot; **(d)** cyclic stability study for 10000 discharge cycles at a constant current density of 8 $A \cdot g^{-1}$ in 2 $mol \cdot L^{-1}$ KOH electrolyte (inset showing first 20 cycles with good charge–discharge behaviour).

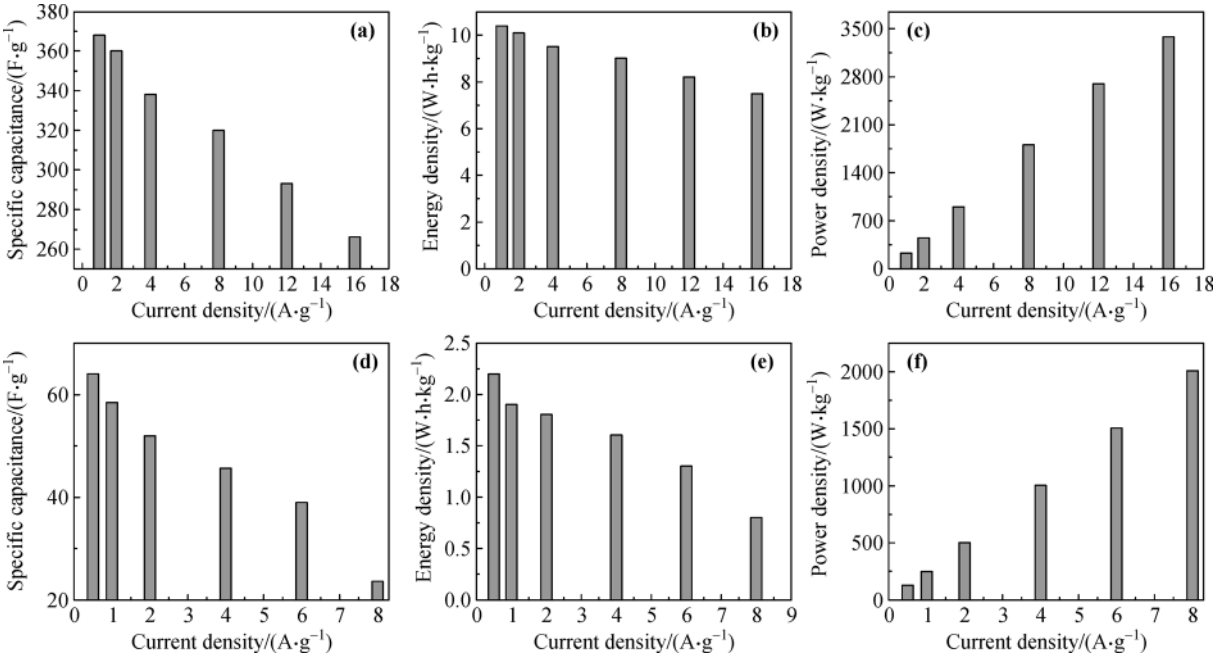

Fig. 9 Comparison of calculated values: **(a)** specific capacitance, **(b)** energy density and **(c)** power density values of the three-electrode system; **(d)** specific capacitance, **(e)** energy density and **(f)** power density values of the symmetrical supercapacitor from GCD curves.

Table 2 Comparison of electrochemical properties of NF supercapacitor device of the present work with that reported in the literature [11,34–37]

Electrode material	Specific capacitance @scan rate	Specific capacitance @current density	Electrolyte	Cyclic stability	Refs.
NF nanoparticles symmetric device	89 $F \cdot g^{-1}$@2 $mV \cdot s^{-1}$	64 $F \cdot g^{-1}$@0.5 $A \cdot g^{-1}$	2 $mol \cdot L^{-1}$ KOH	81% after 10000 cycles @8 $A \cdot g^{-1}$	this work
NF nanosheet	–	236 $F \cdot g^{-1}$@2 $mA \cdot cm^{-2}$	PVA-KOH	98% after 7000 cycles	[11]
$NiFe_2O_4$@rGO	–	139 $F \cdot g^{-1}$@0.5 $A \cdot g^{-1}$	1 $mol \cdot L^{-1}$ KNO_3	92.5% after 6000 cycles @3 $A \cdot g^{-1}$	[34]
$NiFe_2O_4$@rGO hybrid		210.9 $F \cdot g^{-1}$@0.5 $A \cdot g^{-1}$	1 $mol \cdot L^{-1}$ Na_2SO_4	94.2% after 5000 cycles @10 $A \cdot g^{-1}$	[35]
$NiFe_2O_4$@$NiFe_2O_4$//AC asymmetric device	–	–	2 $mol \cdot L^{-1}$ KOH	95.3% after 3000 cycles @10 $mA \cdot cm^{-2}$	[36]
1D $NiFe_2O_4$/graphene composite symmetric device	–	138 $F \cdot g^{-1}$@0.1 $A \cdot g^{-1}$	6 $mol \cdot L^{-1}$ KOH	40% after 10000 cycles @1 $A \cdot g^{-1}$	[37]

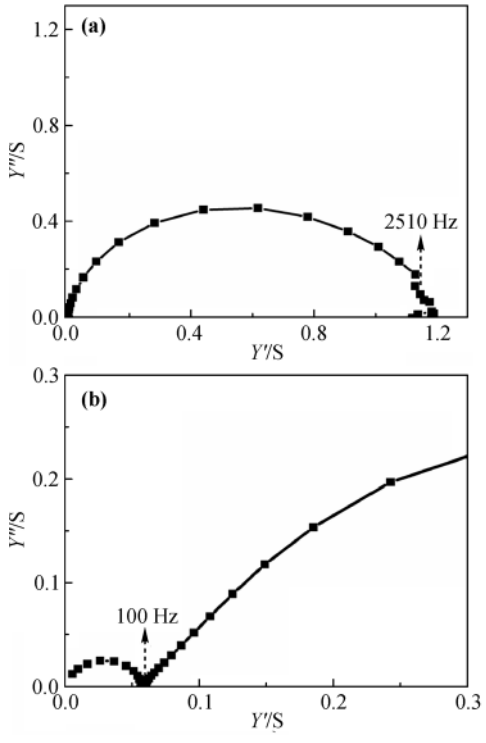

Fig. 10 Admittance plots for NF **(a)** single electrode and **(b)** supercapacitor device.

electrochemical active sites are participating. The obtained values show that nearly 50% of the active sites are involved in the redox reaction. Hence, the obtained high value indicates the active participation of the nano-scale morphology along with contribution from porous nature of the material.

We know that the total capacitance (C_s) is the sum of the capacitance obtained from double-layer capacitance (DLC) and bulk capacitance (pseudocapacitance) which is given by Eq. (7):

$$C_s = C_{DLC} + C_B \quad (7)$$

where, C_{DLC} is the DLC obtained due to the physisorption of electrolyte ions onto the electrode surface, and C_B is the bulk capacitance obtained from the faradaic redox reactions. In order to know the contributions from the capacitive and diffusive controlled process, graphical method is implemented (Fig. 11) [38]. The cumulated capacitance graph of NF in a three-electrode system i.e., capacitance on the *y*-axis *vs.* inverse square root of scan rate in the *x*-axis is presented in Fig. 11(a). It is well known that the surface (EDLC) contribution is dominant when the scan rate tends to infinity, whereas at lower scan rates the bulk (pseudocapacitive) contribution is dominant. For determining the percentage contribution from the surface and bulk process, the lower scan rate points are linearly fitted and higher scan rate points are excluded as they are deviating from the linearity because of the non-effective utilization of the electroactive sites. The intercept is obtained by extrapolating the fitted curve on to the *y*-axis, which provides the pseudocapacitance contribution, and this contribution is subtracted from the total capacitance value in order to obtain the double-layer contribution. The estimated pseudocapacitance contribution is 50.3%, whereas the double layer contribution is 49.7%. Similarly, by following the above procedure, the DLC and pseudocapacitance contribution of NF in a supercapacitor device are 67.9% and 32.1%, respectively (Fig. 11(b)).

4 Conclusions

A facile solvothermal method is applied for the synthesis of NF nanoparticles possessing high surface area. The NF nanoparticles when tested in a three-electrode method

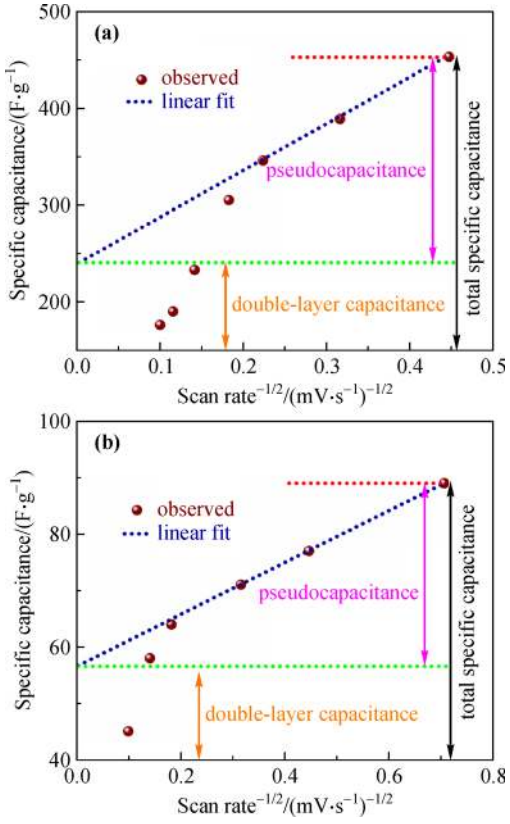

Fig. 11 Graphical determination of capacitance contribution of NF in **(a)** the three-electrode system and **(b)** the fabricated supercapacitor device.

showed a high capacitance value of 478 $F \cdot g^{-1}$ from the CV study at a scan rate of 5 $mV \cdot s^{-1}$ and 368 $F \cdot g^{-1}$ at a current density of 1 $A \cdot g^{-1}$. The electrode material also depicted high energy density value of 10.4 $W \cdot h \cdot kg^{-1}$ and high power density value of 225.8 $W \cdot kg^{-1}$ at the applied current density of 1 $A \cdot g^{-1}$. The life span of the material is tested for 10000 cycles and 88% of the initial capacitance value is retained after the charge–discharge cycles at a high current density of 8 $A \cdot g^{-1}$. The superior electrochemical performance of the nanoparticles is mainly ascribed to the nanoscale morphology with high surface area and high porosity providing substantial electroactive sites for the electrolyte ions insertion/de-insertion apart from sustaining its mechanical stability during the electrochemical process.

References

[1] Sudhakar Y N, Selvakumar M, Bhat D K. Biopolymer Electrolytes: Fundamentals and Applications in Energy Storage. Elsevier, 2018

[2] Sadiq M M J, Shenoy S U, Bhat D K. Novel NRGO–$CoWO_4$–Fe_2O_3 nanocomposite as an efficient catalyst for dye degradation and reduction of 4-nitrophenol. Materials Chemistry and Physics, 2018, 208: 112–122

[3] Peng H, Dai X, Sun K, et al. A high-performance asymmetric supercapacitor designed with a three-dimensional interconnected porous carbon framework and sphere-like nickel nitride nanosheets. New Journal of Chemistry, 2019, 43(32): 12623–12629

[4] Dutta S, Pal S, De S. Mixed solvent exfoliated transition metal oxides nanosheets based flexible solid state supercapacitor devices endowed with high energy density. New Journal of Chemistry, 2019, 43(31): 12385–12395

[5] Sethi M, Bhat D K. Facile solvothermal synthesis and high supercapacitor performance of $NiCo_2O_4$ nanorods. Journal of Alloys and Compounds, 2019, 781: 1013–1020

[6] Pan C, Liu Z, Li W, et al. $NiCo_2O_4$@polyaniline nanotubes heterostructure anchored on carbon textiles with enhanced electrochemical performance for supercapacitor application. The Journal of Physical Chemistry C, 2019, 123(42): 25549–25558

[7] Gao H, Wang X, Wang G, et al. Facile construction of a $MgCo_2O_4$@$NiMoO_4$/NF core–shell nanocomposite for high-performance asymmetric supercapacitors. Journal of Materials Chemistry C: Materials for Optical and Electronic Devices, 2019, 7(42): 13267–13278

[8] Aparna M L, Grace A N, Sathyanarayanan P, et al. A comparative study on the supercapacitive behaviour of solvothermally prepared metal ferrite (MFe_2O_4, M = Fe, Co, Ni, Mn, Cu, Zn) nanoassemblies. Journal of Alloys and Compounds, 2018, 745: 385–395

[9] Kumar P R, Mitra S. Nickel ferrite as a stable, high capacity and high rate anode for Li-ion battery applications. RSC Advances, 2013, 3(47): 25058–25064

[10] Gao X, Wang W, Bi J, et al. Morphology-controllable preparation of $NiFe_2O_4$ as high performance electrode material for supercapacitor. Electrochimica Acta, 2019, 296: 181–189

[11] Bandgar S B, Vadiyar M M, Ling Y C, et al. Metal precursor dependent synthesis of $NiFe_2O_4$ thin films for high-performance flexible symmetric supercapacitor. ACS Applied Energy Materials, 2018, 1(2): 638–648

[12] Hua M, Xu L, Cui F, et al. Hexamethylenetetramine-assisted hydrothermal synthesis of octahedral nickel ferrite oxide nanocrystallines with excellent supercapacitive performance. Journal of Materials Science, 2018, 53(10): 7621–7636

[13] Bhojane P, Sharma A, Pusty M, et al. Synthesis of ammonia-assisted porous nickel ferrite ($NiFe_2O_4$) nanostructures as an electrode material for supercapacitors. Journal of Nanoscience and Nanotechnology, 2017, 17(2): 1387–1392

[14] Anwar S, Muthu K S, Ganesh V, et al. A comparative study of electrochemical capacitive behavior of $NiFe_2O_4$ synthesized by

different routes. Journal of the Electrochemical Society, 2011, 158 (8): A976–A981

[15] Zhang X, Zhang Z, Sun S, et al. A facile one-step hydrothermal approach to synthesize hierarchical core–shell $NiFe_2O_4$@$NiFe_2O_4$ nanosheet arrays on Ni foam with large specific capacitance for supercapacitors. RSC Advances, 2018, 8(27): 15222–15228

[16] Sethi M, Bantawal H, Shenoy U S, et al. Eco-friendly synthesis of porous graphene and its utilization as high performance supercapacitor electrode material. Journal of Alloys and Compounds, 2019, 799: 256–266

[17] Subramanya B, Bhat D K. Novel eco-friendly synthesis of graphene directly from graphite using 2,2,6,6-tetramethylpiperidine 1-oxyl and study of its electrochemical properties. Journal of Power Sources, 2015, 275: 90–98

[18] Giannozzi P, Baroni S, Bonini N, et al. QUANTUM ESPRESSO: a modular and open-source software project for quantum simulations of materials. Journal of Physics: Condensed Matter, 2009, 21(39): 395502

[19] Perdew J P, Burke K, Ernzerhof M. Generalized gradient approximation made simple. Physical Review Letters, 1996, 77 (18): 3865–3868

[20] Shenoy U S, Bantawal H, Bhat D K. Band engineering of $SrTiO_3$: Effect of synthetic technique and site occupancy of doped rhodium. The Journal of Physical Chemistry C, 2018, 122(48): 27567–27574

[21] Sadiq M M J, Shenoy U S, Bhat D K. Enhanced photocatalytic performance of N-doped RGO–$FeWO_4$/Fe_3O_4 ternary nanocomposite in environmental applications. Materials Today Chemistry, 2017, 4: 133–141

[22] Zhao Y, Xu L, Yan J, et al. Facile preparation of $NiFe_2O_4$/MoS_2 composite material with synergistic effect for high performance supercapacitor. Journal of Alloys and Compounds, 2017, 726: 608–617

[23] Sadiq M M J, Shenoy S U, Bhat D K. $NiWO_4$–ZnO–NRGO ternary nanocomposite as an efficient photocatalyst for degradation of methylene blue and reduction of 4-nitro phenol. Journal of Physics and Chemistry of Solids, 2017, 109: 124–133

[24] Wu F, Wang X, Li M, et al. A high capacity $NiFe_2O_4$/RGO nanocomposites as superior anode materials for sodium-ion batteries. Ceramics International, 2016, 42(15): 16666–16670

[25] Cao N, Zou X, Huang Y, et al. Preparation of $NiFe_2O_4$ architectures for affinity separation of histidine-tagged proteins. Materials Letters, 2015, 144: 161–164

[26] Liu L, Sun L, Liu J, et al. Enhancing the electrochemical properties of $NiFe_2O_4$ anode for lithium ion battery through a simple hydrogenation modification. International Journal of Hydrogen Energy, 2014, 39(21): 11258–11266

[27] Subramanya B, Bhat D K. Novel one-pot green synthesis of graphene in aqueous medium under microwave irradiation using a regenerative catalyst and the study of its electrochemical properties. New Journal of Chemistry, 2015, 39(1): 420–430

[28] Zhang Z, Li L, Qing Y, et al. Manipulation of nanoplate structures in carbonized cellulose nanofibril aerogel for high-performance supercapacitor. The Journal of Physical Chemistry C, 2019, 123 (38): 23374–23381

[29] Bhat D K, Shenoy U S. Zn: a versatile resonant dopant for SnTe thermoelectrics. Materials Today Chemistry, 2019, 11: 100158

[30] Shenoy U S, Bhat D K. Electronic structure engineering of tin telluride through co-doping of bismuth and indium for high performance thermoelectrics: a synergistic effect leading to a record high room temperature ZT in tin telluride. Journal of Materials Chemistry C: Materials for Optical and Electronic Devices, 2019, 7(16): 4817–4821

[31] Shenoy U S, Bhat D K. Bi and Zn co-doped SnTe thermoelectrics: interplay of resonance levels and heavy hole band dominance leading to enhanced performance and a record high room temperature ZT. Journal of Materials Chemistry C: Materials for Optical and Electronic Devices, 2020, 8(6): 2036–2042

[32] Kumar N, Kumar A, Huang G M, et al. Facile synthesis of mesoporous $NiFe_2O_4$/CNTs nanocomposite cathode material for high performance asymmetric pseudocapacitors. Applied Surface Science, 2018, 433: 1100–1112

[33] Foo C Y, Lim H N, Mahdi M A B, et al. High-performance supercapacitor based on three-dimensional hierarchical rGO/nickel cobaltite nanostructures as electrode materials. The Journal of Physical Chemistry C, 2016, 120(38): 21202–21210

[34] Zhang X, Zhu M, Ouyang T, et al. $NiFe_2O_4$ nanocubes anchored on reduced graphene oxide cryogel to achieve a 1.8 V flexible solid-state symmetric supercapacitor. Chemical Engineering Journal, 2019, 360: 171–179

[35] Cai Y Z, Cao W Q, Zhang Y L, et al. Tailoring rGO–$NiFe_2O_4$ hybrids to tune transport of electrons and ions for supercapacitor electrodes. Journal of Alloys and Compounds, 2019, 811: 152011

[36] Zhang X, Zhang Z, Sun S, et al. A facile one-step hydrothermal approach to synthesize hierarchical core–shell $NiFe_2O_4$@$NiFe_2O_4$ nanosheet arrays on Ni foam with large specific capacitance for supercapacitors. RSC Advances, 2018, 8(27): 15222–15228

[37] Fu M, Chen W, Zhu X, et al. One-step preparation of one dimensional nickel ferrites/graphene composites for supercapacitor electrode with excellent cycling stability. Journal of Power Sources, 2018, 396: 41–48

[38] Sharma V, Biswas S, Sundaram B, et al. Electrode materials with highest surface area and specific capacitance cannot be the only deciding factor for applicability in energy storage devices: inference of combined life cycle assessment and electrochemical studies. ACS Sustainable Chemistry & Engineering, 2019, 7(5): 5385–5392